Wave impact pressure and kinematics due to breaking wave impingement on a monopile

Mayilvahanan Alagan Chella[1]*, Hans Bihs[1], Dag Myrhaug[2], Øivind Asgeir Arntsen [1],

[1]Department of Civil and Environmental Engineering
[2]Department of Marine Technology
Norwegian University of Science and Technology (NTNU), 7491 Trondheim, Norway

Journal of Offshore Mechanics and Arctic Engineering, 2019, **141**, 051802.

Abstract

Breaking wave impact on a vertical cylinder in shallow waters is investigated numerically with the two-phase flow computational fluid dynamics model REEF3D. The model is based on the incompressible Reynolds-Averaged-Navier-Stokes (RANS) equations together with the level set method (LSM) and $k-\omega$ turbulence model. The spatial and time development of the maximum wave impact pressure and the associated velocity components are examined. Further, the breaking wave characteristics and geometric properties are evaluated with two-dimensional simulations. Comparisons of numerical results and experimental data indicate good agreement for free surface elevations and the characteristics at breaking and the breaking wave forces. A total of 9 two-dimensional and 27 three-dimensional simulations are performed to investigate the influence of the incident wave characteristics, wave impact conditions and breaker types on the maximum wave impact pressure and kinematics. The factors influencing the spatial and temporal variability of the vertical distribution for the maximum impact pressure and kinematics are investigated. Three impact conditions are considered in this study: (1) the wave with a vertical front breaks at the cylinder, (2) the broken wave hits the cylinder with a moderately developed overturning wave crest, and (3) the broken wave impacts the cylinder with a fully developed overturning wave crest. Further, the vertical and longitudinal variations of the maximum impact pressure during the breaking wave impact on the monopile are assessed. The numerically simulated free surface deformations during the wave impact are also presented and discussed. Finally, the total breaking wave force and the maximum impact pressure are analyzed for spilling and plunging b1reakers under different wave impact conditions.

Keywords:

Breaking waves, wave impact pressure, breaking kinematics, breaking characteristics, breaking wave forces, wave impact conditions, spilling and plunging breakers

*Corresponding author

Postprint, published in Journal of Offshore Mechanics and Arctic Engineering, doi: http://dx.doi.org/10.1115/OMAE2016-54451

1 INTRODUCTION

Substructures for offshore wind turbines (OWT) are often exposed to severe hydrodynamic loading particularly from breaking waves. Understanding hydrodynamic loads from breaking waves has many design-related implications for OWT substructures employed in shallow waters Alagan Chella et al. (2012). When deep water waves reach shallow waters, they start to interact with a seabed and break close to the shore. In addition, the energy transfer between different wave frequency components during the process is highly non-linear. Moreover, the wave breaking process is highly influenced by the incident wave characteristics along with environmental conditions such as the water depth and the bottom slope. This adds further challenges to the evaluation of breaking wave forces on structures in shallow waters. Moreover, hydrodynamic loads from breaking waves on OWT substructures in shallow waters and their influence on the global responses still remain uncertain.
The onset of breaking refers to a transition process between the initial wave evolution and the fully broken condition. Thus, the theoretical description of the wave impact loads on strucutres is not straightforward, but the characteristics of breaking waves can be obtained using an empirical breaking criterion Apelt (1987); Babanin (2011). Particularly, impulsive loads from wave breaking against substructures are generally much larger than the quasi-static forces Sawaragi and Nochino (1984). The impact force is characterized by a very impulsive force with a short duration. Its properties depend on the wave characteristics, breaker type, seabed slope and structural configuration Wienke and Oumeraci (2005). In shallow water sites for offshore wind farms e.g. Thornton bank, Belgium, the loads from plunging breaking waves dominate the design stresses of structural elements for a truss structure Alagan Chella et al. (2012).
Several experimental studies have proposed different empirical coefficients to evaluate breaking wave forces for different laboratory breaking conditions Apelt (1987); Goda et al. (1966); Sawaragi and Nochino (1984); Wienke and Oumeraci (2005); Arntsen et al. (2011); Hildebrandt and Schlurmann (2012). For most theoretical models, the information regarding the wave shape and the wave celerity at breaking is required to calculate the breaking wave force. A computational fluid dynamics (CFD) model provides detailed flow information such as the pressure around the structure and the fluid velocities, which are crucial for the evaluation of breaking wave forces on structures. There have been many numerical studies on modeling the interaction of breaking waves with structures and the resulting wave forces (see e.g. Bredmose and Jacobsen (2010); Hildebrandt and Schlurmann (2012); Mo et al. (2013); Bihs et al. (2016*b*); Alagan Chella et al. (2017); Kamath et al. (2016); Ghadirian et al. (2016)). Christensen et al. Christensen et al. (2005) modelled total wave forces and wave run-up on a vertical cyilinder due to breaking waves in shallow waters with a N-S (Navier-Stokes) solver and the VOF (Volume of Fluid) method. Bredmose and Jacobsen Bredmose and Jacobsen (2010) performed simulations with the open-source software OpenFOAM based on the N-S equations and the VOF method for free surface without an explicit turbulence model. Mo et al. Mo et al. (2013) modeled solitary wave breaking and the interaction with a slender cylinder with the filtered N-S equations together with a LES (Large Eddy Simualtion) model with RNG (Renormalization-group) subgrid model. Xiao and Huang Xiao and Huang (2014) investigated breaking solitary waves and the resulting force on a vertical cylinder over a sloping beach using a three-dimensional model that uses the RANS (Reynolds-Averaged Navier-Stokes) equations and the $k-\epsilon$ turbulence model. Recently, Choi et al. Choi et al. (2015) computed the free surface elevation and breaking wave forces on vertical and inclined cylinders using a CFD model based on the N-S equations. The model employs the VOF method for the free surface and the Smagorinsky SGS (sub-grid scale) model for turbulence.

The numerical model REEF3D Bihs et al. (2016*a*) used in the present study has been successfully applied for modelling breaking waves on plane slopes Alagan Chella et al. (2015a, 2016) and over submerged structures Alagan Chella et al. (2015b). The free surface deformation occuring during the breaking process were well represented in the numerical simulations for spilling and plunging breakers over slopes as reported by Alagan Chella et al. Alagan Chella et al. (2016). Further, the model has been validated against large scale laboratory measured data Irschik et al. (2002) for breaking wave forces and the free surface elevation at breaking by Kamath et al. Kamath et al. (2016). The numerical results were in good agreement with the measured data. Further, the study was extended by Bihs et al. Bihs et al. (2016*b*) to examine the effect of wave impact conditions on breaking wave forces on a pair of vertical cylinders placed in tandem arrangement. In addition, the experimentally captured free surface development, the variation of velocity components during the breaking wave impact Mo et al. (2013) and the total breaking wave forces Chakrabarti et al. (1997) are adequately reproduced in the numerical wave tank by Alagan Chella et al. Alagan Chella et al. (2017). The computed results of the above mentioned studies based on REEF3D were consistent with the results of the above mentioned experimental studies. Unlike the previous numerical models, the present numerical model uses higher order numerical schemes for time and spatial discretization which provide a good combination of numerical accuracy and stability.

A number of studies aimed at modelling breaking wave forces have shown quite good results (see e.g. Bredmose and Jacobsen (2010); Mo et al. (2013); Bihs et al. (2016*b*); Alagan Chella et al. (2017); Kamath et al. (2016)). But far too little attention has been paid to investigate wave impact pressure and the associated kinematics associated with breaking wave impacts. These flow quantities are critical in order to understand the wave impact problem which are not yet fully understood. Therefore, the present study attempts to model the vertical variation of wave impact pressure and the velocity components during the breaking wave interaction with a vertical cylinder. Further, the investigation assesses how sensitive the wave impact pressure and the kinematics are to the wave impact conditions.

In the present paper, a numerical investigation of wave impact pressure and velocity during the interaction of a plunging breaking wave with a slender cylinder is carried out with the open-source CFD model REEF3D Bihs et al. (2016*a*). The numerical results for wave surface elevation and the kinematics are compared with experimental data. The pressure, velocity and total breaking wave forces are computed for three different wave impact conditions. As reported by Wienke et al. Wienke et al. (2000), Irschik et al. Irschik et al. (2002) and Kamath et al. Kamath et al. (2016), wave impact force characteristics are largely influenced by the wave breaking condition since the distance between the breaking point and a structure will have a significant effect on the breaking wave forces. Here, three wave impact conditions are considered as shown in Fig. 1 : (A) the wave breaks exactly at the cylinder, (B) the wave breaks before the cylinder and interacts with a fully developed overturning wave crest just below the crest level, and (C) the wave breaks far before the cylinder and impacts with a fully deformed overturning wave crest at the preceding wave trough level. These wave impact conditions are accurately simulated in the numerical wave tank, and the free surface deformations during the interaction with the cylinder are presented and discussed. The vertical variation of pressure and velocity in front of the cylinder and above the still water level are examined for three impact conditions. The maximum pressure and velocity time series are also presented. Further, the computed total wave forces are correlated with the pressure and kinematics.

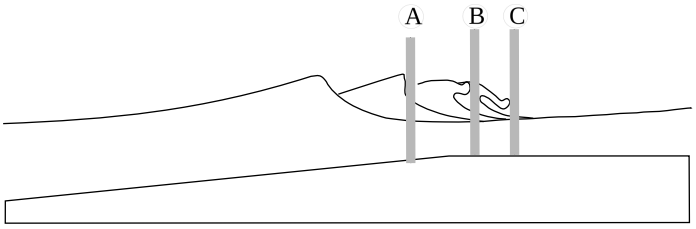

Figure 1: A schematic sketch of three wave impact conditions: (A) When the wave breaks at the cylinder, (B) when the wave breaks before the cylinder and impacts at the wave crest level and (C) when the wave breaks far before the cylinder and hits the cylinder at the preceding wave trough level.

2 NUMERICAL MODEL

In REEF3DBihs et al. (2016*a*), two-phase fluid flow is defined using the incompressible RANS equations together with the continuity equation:

$$\frac{\partial u_i}{\partial x_i} = 0 \tag{1}$$

$$\frac{\partial u_i}{\partial t} + u_j \frac{\partial u_i}{\partial x_j} = -\frac{1}{\rho}\frac{\partial p}{\partial x_i} + \frac{\partial}{\partial x_j}\left[(\nu + \nu_t)\left(\frac{\partial u_i}{\partial x_j} + \frac{\partial u_j}{\partial x_i}\right)\right] + g_i. \tag{2}$$

Here, u is the velocity averaged over time t, p is the pressure, ρ is the fluid density, ν is the kinematic viscosity, ν_t is the eddy viscosity, i and j denote the indices for u and x components in x, y and z directions and g_i is the acceleration due to gravity. The grid architecture in the model is based on two approaches, a uniform Cartesian grid method and a nonuniform grid method with a local grid refinement. The main advantage of the Cartesian grid method is that it allows a straight forward implementation of higher order spatial and temporal discretization schemes that provide very good numerical accuracy and stability for violent free surface flow problems. The spatial discretization is carried out with the fifth-order weighted essentially non-oscillatory (WENO) scheme Jiang and Shu (1996). The third-order accurate TVD Runge-Kutta scheme is employed for the time discretization Shu and Osher (1988). In the simulations, the time step is calculated based on the Courant-Friedrichs-Lewy (CFL) criterion using an adaptive time stepping method Griebel et al. (1998). The projection method Chorin (1968) is used for the pressure treatment. In the first step, the RANS equations are solved without the pressure term and then this term is determined with the Poisson equation using the Jacobi-preconditioned BiCGStab solver. Moreover, in order to establish a strong coupling between pressure and velocity fields, the staggered grid arrangement is employed. The level set method is used to capture the location of the fluid interface and it is defined as the signed distance function $\phi(\vec{x}, t)$ Osher and Sethian (1988). It provides the distance to the interface and also the sign as follows:

$$\phi(\vec{x}, t) \begin{cases} > 0 \ if \ \vec{x} \in water, \\ = 0 \ if \ \vec{x} \in \Gamma, \\ < 0 \ if \ \vec{x} \in air, \end{cases} \tag{3}$$

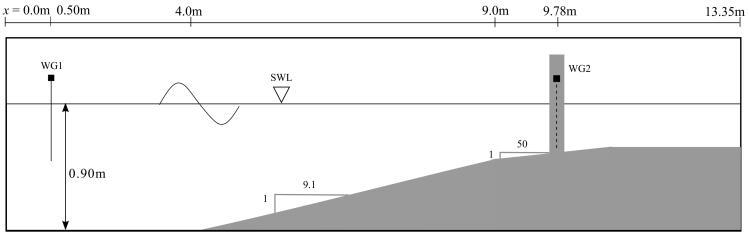

Figure 2: Computational setup for the validation case.

where Γ is the interface between air and water. The level set function is advected by the velocity field:

$$\frac{\partial \phi}{\partial t} + u_j \frac{\partial \phi}{\partial x_j} = 0. \tag{4}$$

The signed distance function satisfies the Eikonal equation $|\nabla \phi| = 1$ in the computational domain. Turbulence under the breaking waves is modeled with the $k-\omega$ model Wilcox (1994). In the wave tank, a relaxation method Larsen and Dancy (1983); Jacobsen et al. (2012) is employed at the inlet boundary for the wave generation. A part of the wave tank is considered for the wave generation at the inlet and the wave absorption at the outlet. The theoretical values are prescribed at the inlet to modulate the computational solution for free surface elevations and velocity with a relaxation function in the relaxation zone Jacobsen et al. (2012). At the outlet boundary, the active beach Schäffer and Klopman (2000) is employed to absorb waves. The wave force is determined by using the pressure p and the viscous stress tensor τ over the surface as follows:

$$F = \int_{\Omega} (-\mathbf{n}p + \mathbf{n}.\tau) d\Omega, \tag{5}$$

where $\mathbf{n}$ is the normal vector to the surface, and Ω is the surface of the structure. A three-dimensional ghost cell immersed boundary method (GCIBM) Berthelsen and Faltinsen (2008) is implemented to model the complex geometries. Parallel computation is employed in the numerical model which is based on the domain decomposition method and MPI (message passing interface).

3 RESULTS AND DISCUSSION

3.1 Validation of Numerical Model

The numerical setup of the computational domain consists of a 4m long flat bed followed by a submerged wedge as shown in Fig. 2; the three-dimensional (3D) numerical wave tank is 18.65m long, 0.4m wide and 1.60m high. The cylinder of diameter D=0.06m is placed at 9.78m from the wave generation zone. The waves are generated by prescribing free surface elevation and velocities of a 5th-order Stokes waves according to Fenton Fenton (1999) at wave inlet with a deep water wave height of H_0=0.24m and a wave period of T=2.22s. Further, the wave propagates over the slope and breaks with a larger overturning wave crest similar to a plunging breaking wave on the flatbed part. The offshore wave steepness (H_0/L_0, L_0 is the deep water wave length) of the plunging breaking waves is 0.031. The computational domain is divided into 12.0 million uniform cells with a grid size dx=0.01m. The grid size is similar to that of Alagan Chella et al. Alagan Chella et al.

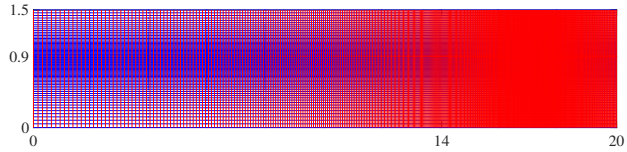

Figure 3: Computational domain with nonuniform grids and local grid refinement (UG-LGR).

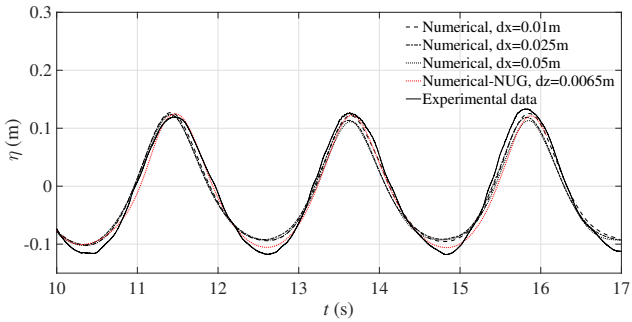

Figure 4: Comparison of numerical and experimental wave surface elevation at x=0.50m (WG 1).

(2017) used to study the breaking wave interaction with a slender cylinder. However, three different grid sizes are tested in order to investigate the grid dependency of the present model for simulating breaking waves. The wave surface elevations are computed at x=0.50m (WG1) and 9.78m (WG2) for four different grid sizes and they are compared with the experimental measurements Arntsen et al. (2011) as presented in Figs. 4 and 5. The wave gauge WG2 is located beside the cylinder at a distance of 0.1m away from the center line ($x-y$ axis) of the wave tank.

The percentage of difference between the numerical results and the experimental data and the number of cells per wavelength (L_0/dx) and wave height (H_0/dx) for three different grid sizes are presented in Table 1. Two different grid arrangements have been employed in the present study. Firstly, a uniform Cartesian grid arrangement (UG) is utilized in the numerical model for the discretization of the computational domain and the grid size is uniform in all three directions (i.e. dx= dy=dz). Then a nonuniform grid arrangement with local grid refinement (NUG-LGR) has been implemented. The grid size varies from 0.0085m close to the tank bottom to 0.0060m around the free surface in the vertical direction (dz) and from 0.010m close to the inlet to 0.075m around the front face of the cylinder in the longitudinal (dx) and lateral directions (dy). Therefore, the grid size of the region of interest, i.e. close to the free surface it is 0.006m in the vertical direction (dz) and in the vicinity of the cylinder it is 0.0075m in the longitudinal (dx) and lateral (dy) directions as shown in Fig. 3. Moreover, the deep water wave length (L_0) of the present case is 7.68m. The simulation with coarser grids has 154 cells per wave length and 16 cells per wave height; the uniform fine grid simulation has 770 cells per wave length and 24 cells per wave height; the nonuniform grids with local refinement case have 1027cells per wave length and 40 cells per wave height.

At x=0.50m (WG1 (Fig. 4)), the computed wave crests are 4.2% and 1.2 % lower than the measured data, but the numerical wave troughs are 18% and 10.3% lower than the measured troughs for the uniform fine grid (dx=0.01m) and the NUG-LGR approach, respectively. Furthermore, at x=9.78m (WG2 (Fig. 5)), the computed wave crests and wave troughs are 4% and 2.9% higher

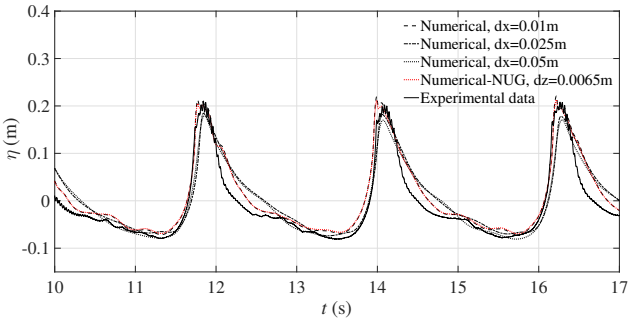

Figure 5: Comparison of numerical and experimental wave surface elevation at x=9.78m (WG2).

Table 1: Comparison of percentage differences between numerical and experimental results for three different uniform grid sizes (dx=0.05m, 0.025m, and 0.01m) and nonuniform grids (dx=0.0075 and dz=0.006). The positive and negative numbers indicate that the numerical results are higher and lower than the experimental results, respectively.

Grid size dx (m)	L_0/dx	H_0/dz	% of difference			
			WG 1		WG 2	
			crest	trough	crest	trough
0.050	154	5	- 8.0	- 21.0	- 10.0	-10.0
0.025	308	10	- 6.0	- 20.0	- 9.0	-10.0
0.010	770	24	- 4.2	-18.0	+ 4.0	- 9.0
LGR	1027	40	-1.2	-10.3	+2.9	-7.9

Table 2: Comparison of percentage differences between numerical and experimental results for three different uniform grid sizes (dx=0.05m, 0.025m, and 0.01m) and nonuniform grids (dx=0.0075m and dz= 0.006m)

and 9% and 7.9% lower than the measured data for the two grid arrangements, respectively. At x=0.50m, the computed wave crests match the measured data, but the numerical wave troughs are slightly lower than the measured troughs. This may be due to the interaction of reflected waves from the slope (not from the beach) with the incoming waves from the wave maker. In the laboratory experiments, the reflected waves are not absorbed at the wave maker whereas they are absorbed in the numerical wave tank with the relaxation method for the wave generation Larsen and Dancy (1983); Jacobsen et al. (2012). In the numerical model, the relaxation method is employed for the wave generation in order to represent the laboratory waves accurately in the numerical wave tank. As the wave propagates over the flat bed after passing the slope, the numerical wave troughs are in good agreement with the experimental data. For the grid sizes dx=0.025m and 0.05m, at WG1 (x=0.50m), the computed wave crests are 6% and 8%, respectively, and the wave troughs are 20% and 21%, respectively, lower than the experimental data; at WG2 (x=9.78m), the numerical wave crests are 9% and 10%, respectively. The computed wave troughs are 10% lower than the measured results for both $dx = 0.025$ m and $dx = 0.05$ m. As can be seen from Table 1, as the number of cells

Results	η_b (m)	H_b (m)	γ_b	Ω_b	C_b (m/s)
Experimental	0.198	0.276	0.83	1.15	2.30
Numerical (UG)	0.208	0.268	0.81	1.12	2.27
Numerical (NUG-LGR)	0.204	0.273	0.83	1.14	2.29

Table 3: Comparison of numerical and experimental results for breaking wave characteristics.

per wave height increases, the difference between the numerical and experimental results decreases for both wave crest and trough predictions.

Although for the case with dx=0.025m is refined by a factor 2 when compared to the case with dx=0.050m, there is no significant improvement noticed. It is also evident from Figs. 4 and 5 for both grid sizes, that the computed wave phase information of wave crests and troughs is consistent with the measured one. Therefore, the coarse grid case with 154 cells per wavelength captures fairly the longitudinal variation of the free surface elevation including the phase information; however, the vertical variation is underestimated. It seems possible that the wave kinematics in the vertical direction is not fully represented. In particular, the flow becomes rotational with an overturning wave crest that is initiated in the upper portion of the wave crest during the breaking process.

With a further refinement of the fine grid case with 24 cells per wave height and 770 cells per wave length, the variation of the free surface elevation during the wave breaking and the breaking wave impacting the cylinder is reasonably well reproducing the experimental results. Then, with the NUG-LGR approach, the numerical solutions around the free surface and the cylinder are refined with 40 cells per wave height and 1027 cells per wave length. Thus, the flow kinematics associated with the longitudinal and vertical transformation of breaking waves are represented quite reasonably and the accuracy of the numerical solution is slightly improved when compared to the uniform grid arrangement. It should be noted that the most prominent flow transformations take place longitudinally and vertically in the vicinity of the free surface during the breaking process. Accordingly, a finer grid resolution is required in both longitudinal and vertical directions in order to represent the complete physical processes including the wave breaking and the interaction with the cylinder. Therefore, both uniform (dx=0.01m) and nonuniform (dx=0.0075m and dz=0.006m) grids are chosen. When the wave propagates over the submerged slope it undergoes the shoaling process. As a result, the wave height increases and reaches its maximum value just before breaking. In particular, the symmetrical incident wave profile completely transforms into an asymmetric wave profile with a narrower and a larger wave crest and a wider and a shallower wave trough. These asymmetric wave profiles including the wave troughs at breaking are reasonably well represented in the numerical simulation. Finally, the wave breaks exactly at the cylinder, i.e. the wave hits the cylinder exactly with a nearly vertical wave front as shown in Fig. 1 for wave impact condition A. This is also consistent with the experimentally observed flow features. Overall, the computed wave surface elevations at both wave gauge locations are in good agreement with the measurements.

Further, the numerically calculated breaking wave characteristics are compared with the experimental data as listed in Table 3.1. The computed wave characteristics such as the wave surface elevation (η_b=0.208m) and the wave height at breaking (H_b=0.268m) are 5% and 3% higher and 2.8% and 1% lower than the experimentally measured values for the uniform (dx=0.01m) and nonuniform

(dx=0.0075m and dz=0.006m) grids, respectively. In addition, the calculated breaker depth index ($\gamma_b = H_b/d_b$, where d_b is the water depth at breaking) and breaker height index ($\Omega_b = H_b/H_0$, where H_0 is the deep water wave height) are almost the same as those of the experiments. At the onset of breaking, the flow condition corresponds to a transition phase of the breaking process. It is important to model the wave celerity at breaking (C_b) correctly as this also determines the development of the wave crest during the breaking process. In the numerical simulation, C_b is 2.27 m/s for dx=0.010m and 2.30m/s for dz=0.006mm, which are very close to the experimentally calculated value (C_b=2.30 m/s). With the nonuniform grid arrangement, the breaking characteristics (γ_b and Ω_b) and C_b are calculated accurately (Table 3.1). Therefore, the nonuniform grid arrangement with local grid refinement is considered for the numerical experiments. The comparison between the numerical and experimental results clearly shows that the numerical model predicts the breaker height and location accurately including the wave celerity at breaking.

3.2 Vertical Distribution of Wave Impact Pressures and Kinematics

For the given incident wave characteristics, the intensity of the wave impact mainly depends on the distance between the breaking point and the cylinder Kamath et al. (2016); Bihs et al. (2016*b*). The study focuses on investigating the distribution of wave impact pressure and kinematics in front of the cylinder for three different wave impact conditions: the wave breaks at the cylinder (Condition A), the wave breaks before the cylinder and impacts just below the wave crest level (Condition B), and the wave breaks far before the cylinder and hits the cylinder at the preceding wave trough level (Condition C) as presented in Fig. 1. The wave characteristics and kinematics of a wave vary significantly during the complete cycle of the breaking process. Therefore, a two-dimensional simulation is carried out to determine the breaking location and to assess the different stages of the wave breaking process. Further, in the 3D setup, a total of 6 simulations based on the NUG-LGR arrangement are performed for three wave impact conditions simulated by changing the position of the cylinder with respect to the breaking point. Figs. 6, 7 and 8 present the numerically captured free surface deformations for conditions A, B and C, respectively. It should be noted that the flow scenarios around the cylinder are completely different for each wave impact conditions.

Fig. 9 shows the computed maximum pressure (p) in front of the cylinder versus the normalized height (z/η_{max}) above the still water level for the NUG-LGR arrangement (η_{max} is the maximum wave surface elevation). The maximum impact pressures (p) are 4.80 kPa, 6.24 kPa, 4.54 kPa (dz=0.006m) for conditions A, B, C, respectively. It appears that the vertical maximum pressure distribution almost follows the deformed shape of the wave crest for conditions A (Fig. 6) and B (Fig. 7). A drastic increase in the wave height takes place when the wave approaches the breaking point. Therefore, the particle velocities near the wave crest region increase resulting in a nearly vertical wave front at the breaking point. For condition A, the wave breaks exactly onto the cylinder and the pressure distribution in Fig. 9 looks almost similar to the wave shape in the $x-z$ plane (Fig. 6). After the breaking point, the wave front starts to curl forward and evolves into an overturning water jet as depicted in Fig. 7. The vertical pressure distribution for condition B resembles the wave profile shape at the impact. Moreover, the velocity magnitude is maximum around 0.6 z/η_{max} and the maximum horizontal particle velocity (u) occurs as the pressure at z/η_{max}=0.6. Initially, the pressure in front of the cylinder increases as z increases and it reaches the maximum value at z/η_{max}= 0.58, 0.58 and 0.46 for conditions A, B and C, respectively. It is possible that the most intensive wave impacts take place at these levels. Although the wave impact conditions are different for conditions $A$and B, the maximum pressure occurs at the same level.

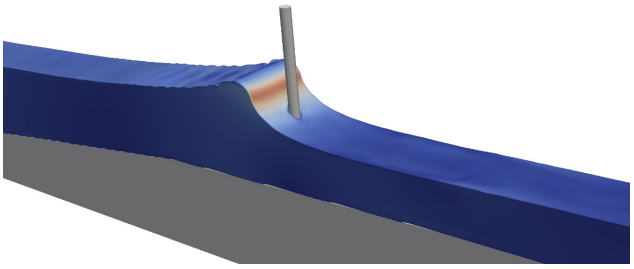

(a) t=10.20s

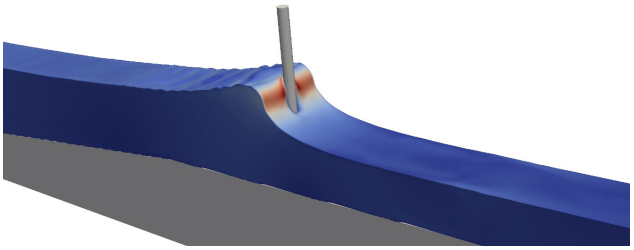

(b) t=10.25s

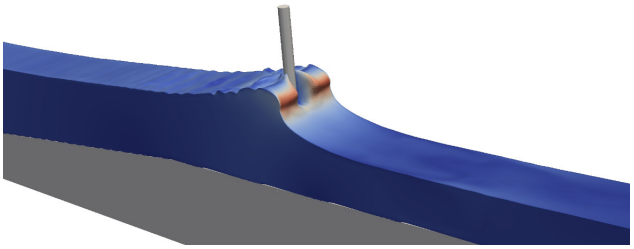

(c) t=10.30s

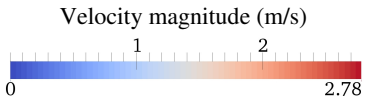

Figure 6: Simulated free surface flow features with velocity magnitude (m/s) variation for wave impact condition A.

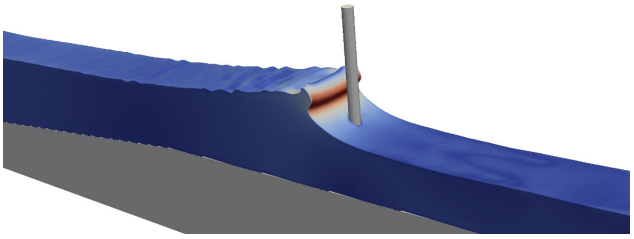

(a) t=10.40s

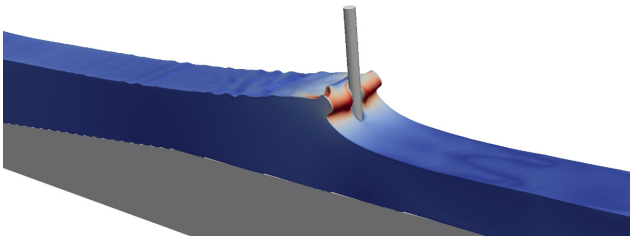

(b) t=10.45s

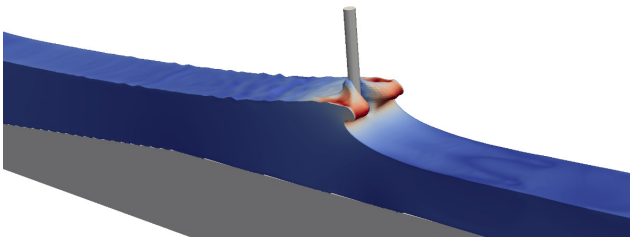

(c) t=10.50s

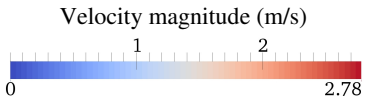

Figure 7: Simulated free surface flow features with velocity magnitude (m/s) variation for wave impact condition B.

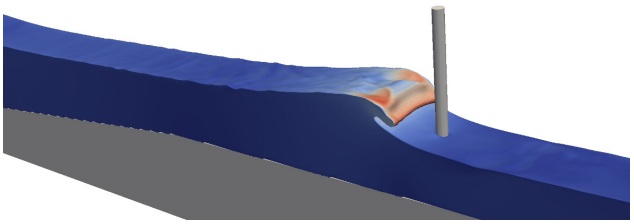

(a) t=10.60s

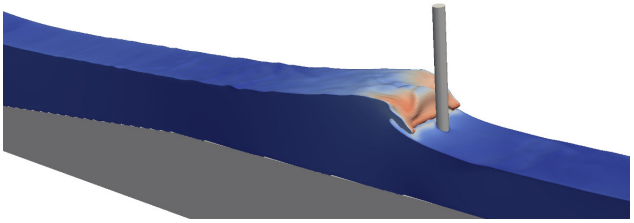

(b) t=10.65s

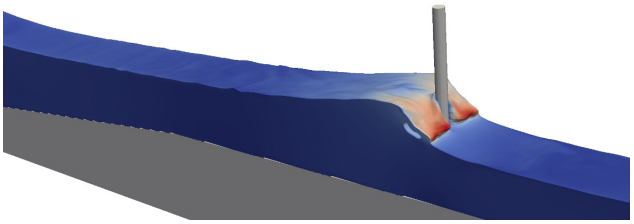

(c) t=10.70s

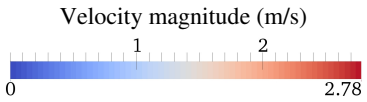

Figure 8: Simulated free surface flow features with velocity magnitude (m/s) variation for wave impact condition C.

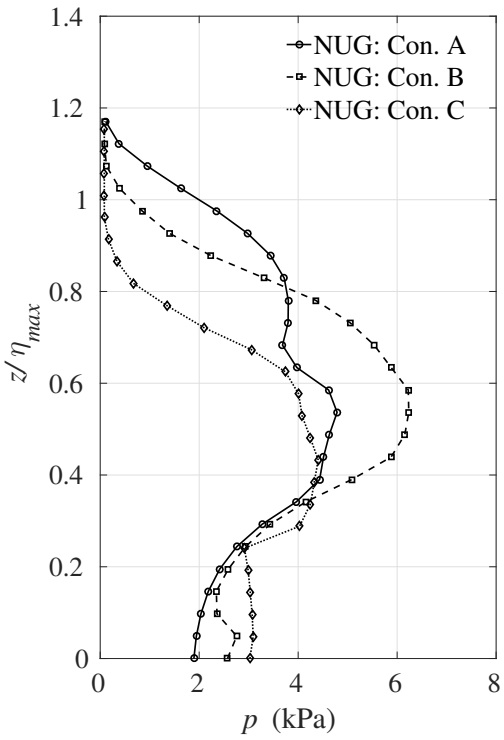

Figure 9: Distribution of wave impact pressure on the cylinder versus the normalized wave surface elevation for NUG-LGR (dx=0.0075m and dz=0.006m) for three impact conditions: A(solid line), B(dashed line) and C(dotted line).

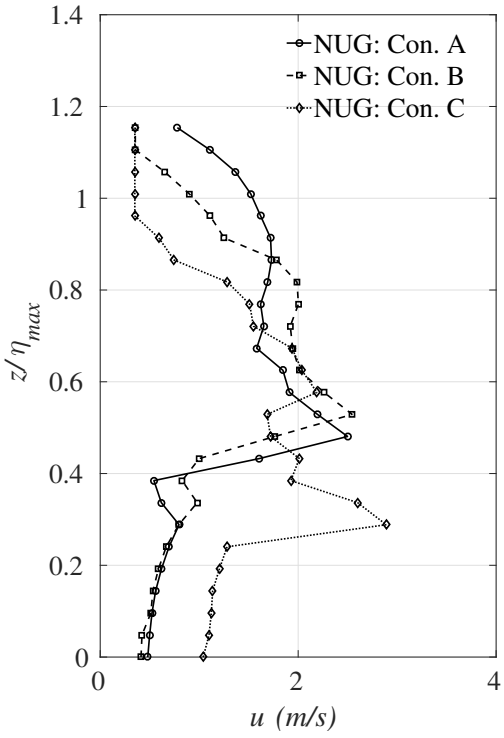

Figure 10: Distribution of horizontal velocity component in front of the cylinder versus the normalized wave surface elevation for NUG-LGR (dx=0.0075m and dz=0.006m) for three impact conditions: A(solid line), B(dashed line) and C(dotted line).

At the onset of breaking, the wave front becomes vertical and most of the wave energy contribute to increasing the potential energy of the wave. Also, the development of the overturning wave crest is visible in Fig. 6. In addition, the maximum velocity magnitude does not occur at the top of the wave crest, but in the middle of the wave crest as shown in Fig. 6 (a) and (b). Further, the overturning wave crest evolves into fully developed condition and it hits the cylinder just below the crest level. Similar to condition A, the velocity magnitude is maximum in the middle portion of the overturning wave crest (Fig. 7 (a) and (b)). Whereas in the case of condition C, the overturning wave crest is fully deformed and it impacts the cylinder at the forward trough level (Fig. 8). Therefore, the maximum pressure is more likely to occur at a lower z.

Figs. 10 and 11 present the vertical distribution of maximum horizontal and vertical components of velocity versus the normalized height (z/η_{max}) on the cylinder. The horizontal (u) and vertical (w) components of velocity are computed vertically at each level when the pressure is maximum. In this case, the maximum horizontal velocity occurs at z/η_{max}=0.58 (2.40 m/s), 0.58 (2.53 m/s) and 0.29 (2.81 m/s) for conditions A, B and C, respectively. For condition $A$and B, the vertical profile of horizontal velocity nearly follows the vertical pressure profile. For condition B, the maximum values for p and u occur at z/η_{max}=0.58. However, for condition A, the largest u occurs at z/η_{max}=0.48 which is lower than the position of largest p (z/η_{max}=0.58). Similarly, for condition C, the largest u appears at z/η_{max}=0.29 while the largest pressure appears at z/η_{max}=0.48. Though the maximum u appears at the level lower than the other conditions, the largest u occurs for condition C.

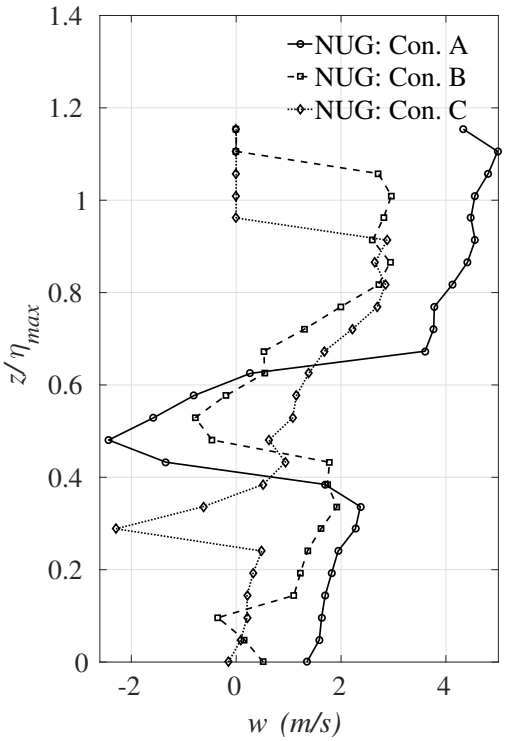

Figure 11: Distribution of vertical velocity component in front of the cylinder versus the normalized wave surface elevation for NUG-LGR (dx=0.0075m and dz=0.006m) for three impact conditions: A(solid line), B(dashed line) and C(dotted line).

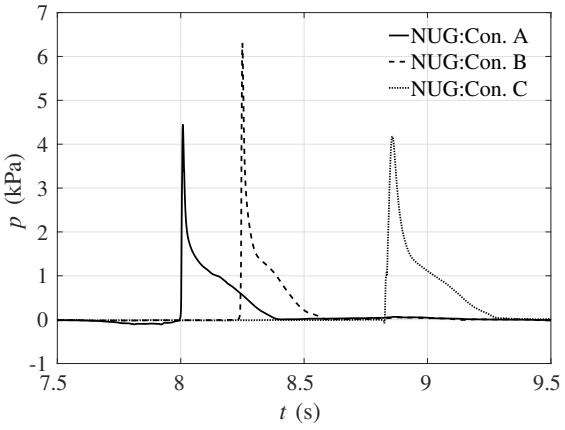

Figure 12: Wave impact pressure versus time for NUG-LGR (dx=0.0075m and dz=0.006m) for three impact conditions: A(solid line), B(dashed line) and C(dotted line).

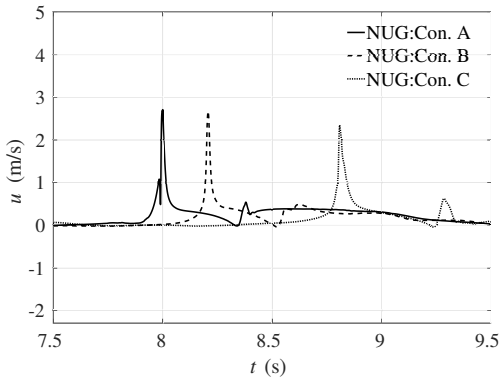

Figure 13: Horizontal velocity component versus time for NUG-LGR (dx=0.0075m and dz=0.006m) for three impact conditions: A(solid line), B(dashed line) and C(dotted line).

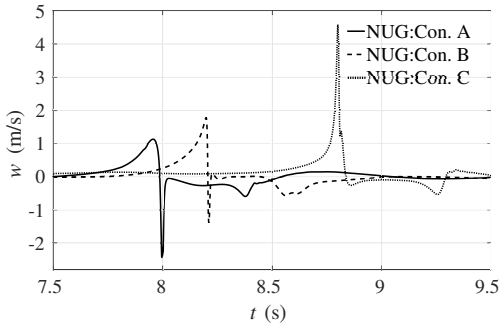

Figure 14: Vertical velocity component versus time for NUG-LGR (dx=0.0075m and dz=0.006m) for three impact conditions: A(solid line), B(dashed line) and C(dotted line).

The maximum vertical velocity appears at z/η_{max}=1.106 (4.485 m/s), 0.86 (2.98 m/s) and 0.81 (2.96 m/s) for conditions A, B and C, respectively. As cab be seen in Figs. 9 and 10, the vertical distribution of w over the depth does not follow the distributions of p and u. For condition A, the maximum w occurs almost at the tip of the wave crest and it increases gradually from the still water level. In general, z/η_{max} at the maximum of w is always higher than for the maximum of u. The vertical w profile for NUG-LGR includes small flow details around the cylinder with the refinement of grid sizes in the longitudinal and vertical directions. Figs. 12, 13 and 14 show pressure and horizontal and vertical components of velocity versus time at z/η_{max}=0.58 (A), 0.58 (B) and 0.48 (C) for three impact conditions. The pressure variation for condition B is sharper and higher than for the other two conditions which is due to the impact of the fully developed overturning wave crest (Fig. 7). In addition, the pressure rise time is 0.012s, 0.009s and 0.020s for conditions A, B and C, respectively. In the case of condition B, the overturning wave crest starts to evolve when the most potential energy turns into kinetic energy in addition to the existing wave energy under the wave crest. As a result, the overturned wave crest hits the structure with high velocity (Fig. 7 (a)). It should be noted that the maximum pressure and horizontal velocity occur at the same level

Impact conditions	Time in s		
	For p	For u	For w
Condition A	8.04	7.96	7.90
Condition B	8.35	8.25	8.20
Condition C	8.90	8.82	8.70

Table 4: Comparison of time at which the peak occurs for pressure, horizontal and vertical components of velocity for three wave impact conditions.

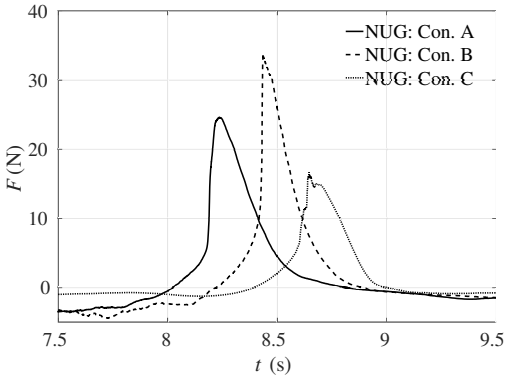

Figure 15: Breaking wave forces on the cylinder for NUG-LGR (dx=0.0075m and dz=0.006m) for three impact conditions: A(solid line), B(dashed line) and C(dotted line).

(z/η_{max}=0.58).

For all conditions, considering the time scale, w first reaches the maximum value followed by u, and then p as presented in Table 3.2. In contrast to w, u and p follow the same trend i.e. the maximum value for p and u occurs sharply with a very short rise time, decreasing gradually after attaining the maximum value (Figs. 12, 13 and 14). Besides, the largest w occurs for condition C. For condition C, the overturning wave crest is fully deformed with high velocity magnitude at the peak and it impinges onto the cylinder surface at the preceding trough level (Fig. 8). During the interaction with the cylinder, w becomes negative (upward velocity is positive and downward velocity is negative) after reaching the peak value for conditions A and B. It should be noted that the w variation seems to be more sensitive to the spatial and temporal variations than for the u variation.

Fig. 15 shows the computed total wave force versus time for three wave impact conditions. The largest wave force occurs for condition B and the lowest for condition C, which is also consistent with the results reported by Kamath et al. Kamath et al. (2016) and Bihs et al. Bihs et al. (2016*b*). For UG, it appears that the wave force curve is sharper and higher for condition B which is also similar to the pressure-time profile (Fig. 12). This flow scenario during the interaction of the overturning wave crest with the cylinder is presented in Fig. 7 for three different time instants. For condition C, the force curve has two peaks due to the impact of the fully deformed overturning wave crest followed by the main wave crest as depicted in Fig. 8. This feature is also observed in the

large scale laboratory experiments performed by Wienke et al. Wienke et al. (2000). In this case, the broken wave loses most of its energy before reaching the cylinder. However, this flow condition causes different wave impact characteristics.

4 SUMMARY AND CONCLUSIONS

A numerical investigation of wave impact pressures and kinematics is carried out with the open-source CFD model REEF3D. The numerical model is based on the Reynolds-Averaged Navier-Stokes (RANS) equations together with the level set method for the free surface and the $k-\omega$ model for the turbulence. First, the numerical results are compared against the experimental measurements for wave surface elevations and kinematics. The numerically simulated wave surface elevations and kinematics are in good agreement with experimental data. Numerical experiments of a plunging breaking wave interaction with a vertical cylinder in a three-dimensional wave tank are performed for two grid arrangements and three different wave impact conditions for the grid refinement study. The two grid arrangements are: (1) based on uniform grid cells and (2) based on the local grid refinement method. The wave impact conditions are (A) when the wave breaks at the cylinder, (B) when the wave breaks before the cylinder, and (C) when the wave breaks far before the cylinder. These impact conditions are numerically modeled. The free surface deformations during the interaction with the cylinder for each wave impact condition are also presented and discussed. For each wave impact condition, the vertical distributions of maximum pressure in front of the cylinder above the still water are computed and the corresponding horizontal and vertical velocity components are calculated. Further, the time series of pressure, horizontal and vertical velocity and total wave force are also examined. As a function of time, the vertical velocity first reaches its maximum value followed by the horizontal velocity and then the pressure. Moreover, the vertical distribution of horizontal velocity follows the distribution of pressure, whereas the vertical velocity distribution does not follow the trend of the pressure. The largest pressure and total wave force occur when the overturning wave crest impacts the cylinder just below the crest level. When the overturning wave crest impacts the cylinder at the crest level(condition B), the pressure and wave force peaks are sharper and higher than the other two impact conditions (conditions A and C). Particularly, the pressure rise time is also shorter. The largest vertical velocity occurs when the wave breaks far before the cylinder. The level at which the maximum horizontal velocity occurs is generally lower than the levels of maximum vertical velocity.

Finally, the computations of the breaking wave characteristics, impact pressures and velocity components and the total breaking wave forces are improved to a certain extent by implementing local grid refinement around the free surface and the cylinder. In the laboratory experiments considered in the present study, the total force and pressure measurements were not performed. Future work will focus on evaluating the numerical code for modelling the distribution of wave impact pressure and force over the depth above the still water level. Further, the time and spatial evolution of pressure and velocity profiles will be examined with the local mesh refinement approach. Also, the wave impact force characteristics and the associated parameters such as the curling factor and the slamming coefficient will be investigated along with the free surface flow characteristics during the breaking process.

Acknowledgment

The research work has been funded by the Research Council of Norway through the project "Hydrodynamic Loads on Offshore Wind Turbine Substructures due to Nonlinear Irregular Breaking, High Steep and Extreme Waves" (project number: 246810). The authors gratefully acknowledge the computing time granted by NOTUR (project number: NN2620K).

References

Alagan Chella, M., Bihs, H. and Myrhaug, D. (2015b). Characteristics and profile asymmetry properties of waves breaking over an impermeable submerged reef. *Coast. Eng.*, **100**, 26–36.

Alagan Chella, M., Bihs, H., Myrhaug, D. and Muskulus, M. (2015a). Breaking characteristics and geometric properties of spilling breakers over slopes. *Coast. Eng.*, **95**, 4–19.

Alagan Chella, M., Bihs, H., Myrhaug, D. and Muskulus, M. (2016). Hydrodynamic characteristics and geometric properties of plunging and spilling breakers over impermeable slopes. *Ocean Modelling*, **103**, 53–72.

Alagan Chella, M., Bihs, H., Myrhaug, D. and Muskulus, M. (2017). Breaking solitary waves and breaking wave forces on a vertically mounted slender cylinder over an impermeable sloping seabed. *Journal of Ocean Engineering and Marine Energy*, **3**, 1–19.

Alagan Chella, M., Tørum, A. and Myrhaug, D. (2012). An overview of wave impact forces on offshore wind turbine substructures. *Energy Procedia*, **20**, 217–226.

Apelt, C. J.and Piorewicz, J. (1987). Laboratory studies of breaking wave forces acting on vertical cylinders in shallow water. *Coast. Eng.*, **11**, 263–282.

Arntsen, Ø.A., Ros, X. and Tørum, A. (2011). Impact forces on a vertical pile from plunging breaking waves. In: *Proceedings of the 24-th Conference on Coastal structures.*

Babanin, A.V. (2011). *Breaking and dissipation of ocean surface waves.* Cambridge University Press.

Berthelsen, P.A. and Faltinsen, O.M. (2008). A local directional ghost cell approach for incompressible viscous flow problems with irregular boundaries. *J. Comput. Phys.*, **227**, 4354–4397.

Bihs, H., Kamath, A., Alagan Chella, M., Aggarwal, A. and Arntsen, Ø.A. (2016*a*). A new level set numerical wave tank with improved density interpolation for complex wave hydrodynamics. *Computers and Fluids*, **140**, 191–208.

Bihs, H., Kamath, A., Alagan Chella, M. and Arntsen, Ø.A. (2016*b*). Breaking wave interaction with tandem cylinders under different impact scenarios. *J. Waterw. Port Coast. Ocean Eng.* DOI: 10.1061/(ASCE)WW.1943-5460.0000343.

Bredmose, H. and Jacobsen, N.G. (2010). Breaking wave impacts on offshore wind turbine foundations: Focused wave groups and CFD. In: *Proceedings of the 29-th International Conference on Ocean, Offshore and Arctic Engineering*, 397–404.

Chakrabarti, S.K., Kriebel, D. and Berek, E. (1997). Forces on a single pile caisson in breaking waves and current. *Appl Ocean Res*, **19**, 113–140.

Choi, S., Lee, K. and Gudmestad, O. (2015). The effect of dynamic amplification due to a structures vibration on breaking wave impact. *Ocean Eng.*, **96**, 8–20.

Chorin, A. (1968). Numerical solution of the Navier-Stokes equations. *Math. Comput.*, **22**, 745–762.

Christensen, E.D., Bredmose, H. and Hansen, E.A. (2005). Extreme wave forces and wave run-up on offshore windturbine foundations. In: *Proceedings of Copenhagen Offshore Wind*, 1–10.

Fenton, J.D. (1999). *The cnoidal theory of water waves*, chapter 2, 55–100. Developments in Offshore Engineering, Gulf, Houston. Herbich. J. B. (Ed.) edition.

Ghadirian, A., Bredmose, H. and Dixen, M. (2016). Breaking phase focused wave group loads on offshore wind turbine monopiles. In: *Journal of Physics: Conference Series*, volume 753.

Goda, Y., Haranaka, S. and Kitahata, M. (1966). Study of impulsive breaking wave forces on piles. Technical report, Port and Harbor Research Institute, Ministry of Transport.

Griebel, M., Dornseifer, T. and Neunhoeffer, T. (1998). *Numerical Simulation in Fluid Dynamics, a Practical Introduction*. SIAM.

Hildebrandt, A. and Schlurmann, T. (2012). Breaking wave kinematics, local pressures, and forces on a tripod structure. In: *Proceedings of the 33rd Conference on Coastal Engineering*, 1–14.

Irschik, K., Sparboom, U. and Oumeraci, H. (2002). Breaking wave characteristics for the loading of a slender pile. In: *Proceedings of the 28-th Conference on Coastal Engineering*, 1341–1352.

Jacobsen, N.G., Fuhrman, D.R. and Fredsøe, J. (2012). A wave generation toolbox for the open-source CFD library : OpenFoam. *Int. J. Numer. Methods Fluids*, **70**, 1073–1088.

Jiang, G.S. and Shu, C.W. (1996). Efficient implementation of weighted ENO schemes. *J. Comput. Phys.*, **126**, 202–228.

Kamath, A., Alagan Chella, M., Bihs, H. and Arntsen, Ø.A. (2016). Breaking wave interaction with a vertical cylinder and the effect of breaker location. *Ocean Eng.*, **128**, 105–115.

Larsen, J. and Dancy, H. (1983). Open boundaries in short wave simulations - a new approach. *Coast. Eng.*, **7**, 285–297.

Mo, W., Jensen, A. and Liu, P.L.F. (2013). Plunging solitary wave and its interaction with a slender cylinder on a sloping beach. *Ocean Eng.*, **74**, 48–60.

Osher, S. and Sethian, J.A. (1988). Fronts propagating with curvature-dependent Speed: Algorithms based on Hamilton-Jacobi formulations. *J. Comput. Phys.*, **79**, 12–49.

Sawaragi, T. and Nochino, M. (1984). Impact forces of nearly breaking waves on a vertical circular cylinder. *Coastal Engineering Journal*, **27**, 249–263.

Schäffer, H.A. and Klopman, G. (2000). Review of multidirectional active wave absorption methods. *J. Waterw. Port Coast. Ocean Eng.*, **126**, 88–97.

Shu, C.W. and Osher, S. (1988). Efficient implementation of essentially non-oscillatory shock capturing schemes. *J. Comput. Phys.*, **77**, 439–471.

Wienke, J. and Oumeraci, H. (2005). Breaking wave impact force on a vertical and inclined slender pile-theoretical and large-scale model investigations. *Coast. Eng.*, **52**, 435–416.

Wienke, J., Sparboom, U. and Oumeraci, H. (2000). Breaking wave impact on a slender cylinder. In: *Proceedings of the 27-th Conference on coastal engineering.*

Wilcox, D.C. (1994). *Turbulence Modeling for CFD.* DCW Industries Inc., La Canada, California.

Xiao, H. and Huang, W. (2014). Three-dimensional numerical modeling of solitary wave breaking and force on a cylinder pile in a coastal surf zone. *J. Eng. Mech. - ASCE*, **141(8)**.